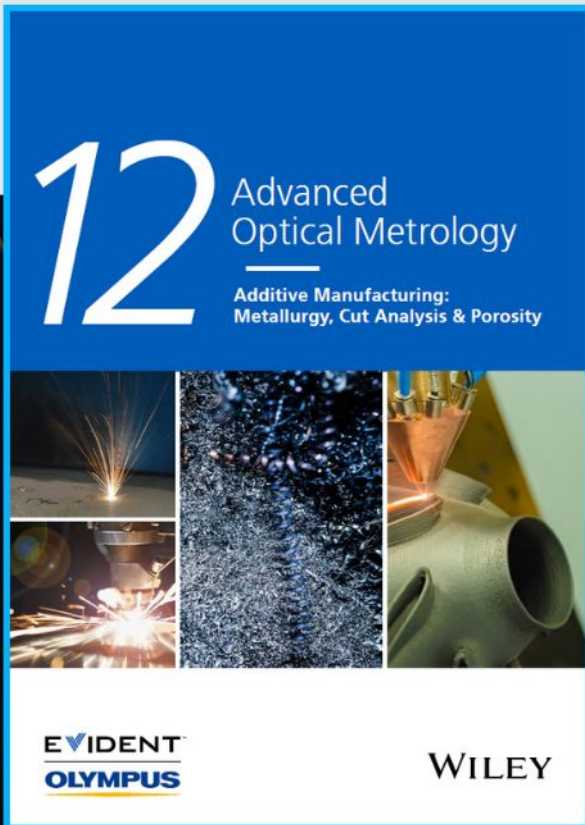




# Additive Manufacturing: Metallurgy, Cut Analysis & Porosity



The latest eBook from  
**Advanced Optical Metrology.**  
Download for free.

In industry, sector after sector is moving away from conventional production methods to additive manufacturing, a technology that has been recommended for substantial research investment.

Download the latest eBook to read about the applications, trends, opportunities, and challenges around this process, and how it has been adapted to different industrial sectors.

**EVIDENT**  
**OLYMPUS**

**WILEY**

# The Edge Effects Boosting Hydrogen Evolution Performance of Platinum/Transition Bimetallic Phosphide Hybrid Electrocatalysts

Yeshu Tan, Jianrui Feng, Haobo Dong, Longxiang Liu, Siyu Zhao, Feili Lai, Tianxi Liu, Ying Bai, Ivan P. Parkin,\* and Guanjie He\*

Platinum (Pt) is regarded as a promising electrocatalyst for hydrogen evolution reaction (HER). However, its application in an alkaline medium is limited by the activation energy of water dissociation, diffusion of H<sup>+</sup>, and desorption of H<sub>2</sub>. Moreover, the formation of effective structures with a low Pt usage amount is still a challenge. Herein, guided by the simulation discovery that the edge effect can boost local electric field (LEF) of the electrocatalysts for faster proton diffusion, platinum nanocrystals on the edge of transition metal phosphide nanosheets are fabricated. The unique heterostructure with ultralow Pt amount delivered an outstanding HER performance in an alkaline medium with a small overpotential of 44.5 mV and excellent stability for 80 h at the current density of  $-10 \text{ mA cm}^{-2}$ . The mass activity of as-prepared electrocatalyst is  $2.77 \text{ A mg}^{-1}_{\text{Pt}}$ , which is 15 times higher than that of commercial Pt/C electrocatalysts ( $0.18 \text{ A mg}^{-1}_{\text{Pt}}$ ). The density function theory calculation revealed the efficient water dissociation, fast adsorption, and desorption of protons with hybrid structure. The study provides an innovative strategy to design unique nanostructures for boosting HER performances via achieving both synergistic effects from hybrid components and enhanced LEF from the structural edge effect.

Hydrogen, as a type of clean energy with a high energy density of  $\approx 142 \text{ MJ kg}^{-1}$ , has been regarded as a promising energy alternative to fossil fuels due to its rapid development of production, storage, and transport.<sup>[2]</sup> Hydrogen is also carbon-free and environmentally friendly.<sup>[3]</sup> To date, water electrolysis is recognized as a rational and sustainable strategy to produce hydrogen. The entire water electrolysis consists of two half-reactions, hydrogen evolution reaction (HER) and oxygen evolution reaction (OER).<sup>[4]</sup> The HER process undergoes three steps, i.e., Volmer step, Heyrovsky step, and Tafel step. An efficient and durable electrocatalyst is vital for HER.<sup>[5]</sup>

Noble metal materials are regarded as top candidates for HER electrocatalysts due to their hydrogen adsorption energy close to zero, therefore is beneficial for hydrogen intermediates adsorption.<sup>[6]</sup> Platinum is highly preferential for HER, but its high cost and scarcity lead to many restrictions for future applications.<sup>[7]</sup> Thus, numerous types of methods were processed to increase the HER performance and lower the usage amount of the Pt. Pt quantum dots,<sup>[8]</sup> nanowires,<sup>[9]</sup> nanoclusters,<sup>[10]</sup> and nanostars<sup>[11]</sup> were fabricated to

## 1. Introduction

The increasing energy consumption and greenhouse gas emission make it urgent to develop sustainable energy resources.<sup>[1]</sup>

Y. Tan, J. Feng, H. Dong, L. Liu, S. Zhao, I. P. Parkin, G. He  
Christopher Ingold Laboratory  
Department of Chemistry  
University College London  
20 Gordon Street, London WC1H 0AJ, UK  
E-mail: i.p.parkin@ucl.ac.uk; g.he@ucl.ac.uk  
F. Lai  
Department of Chemistry  
KU Leuven  
Celestijnenlaan 200F, Leuven 3001, Belgium

 The ORCID identification number(s) for the author(s) of this article can be found under <https://doi.org/10.1002/adfm.202209967>.

© 2022 The Authors. Advanced Functional Materials published by Wiley-VCH GmbH. This is an open access article under the terms of the Creative Commons Attribution License, which permits use, distribution and reproduction in any medium, provided the original work is properly cited.

T. Liu  
Key Laboratory of Synthetic and Biological Colloids  
Ministry of Education  
School of Chemical and Material Engineering  
International Joint Research Laboratory for Nano Energy Composites  
Jiangnan University  
Wuxi 214122, P. R. China  
Y. Bai  
School of Physics & Electronics  
Henan University  
Kaifeng 475004, P. R. China  
G. He  
Electrochemical Innovation Laboratory  
Department of Chemical Engineering  
University College London  
London WC1E 7JE, UK

DOI: 10.1002/adfm.202209967

increase the electrochemical active surface area, thus boosting the density of active sites. However, Pt-based electrocatalysts were limited under alkaline conditions. The suppressed HER activity of Pt is attributed to sluggish water dissociation, leading to slow H<sup>+</sup> diffusion.<sup>[12]</sup> Meantime, Pt with strong adsorption of H\* is limited by H\* desorption in Tafel step.<sup>[13]</sup> Thus, forming heterostructures is a promising strategy to deliver synergistic effects and boost HER performance in an alkaline medium. The Pt islands were grown directly on Ni nanoparticles as efficient HER electrocatalysts.<sup>[14]</sup> The highly strained Pt nanocrystals on Ni nanoparticles led to fast hydrogen desorption and increased mass activity. The overpotential reached 49 mV at the current density of -10 mA cm<sup>-2</sup>, and the mass activity is 10.5 times higher than that of the commercial Pt/C. Additionally, Pt located on Ni(HCO<sub>3</sub>)<sub>2</sub> was reported as a heterostructure electrocatalyst to accelerate the HER.<sup>[13a]</sup> The Ni(HCO<sub>3</sub>)<sub>2</sub> served as the substrate for uniform dispersion of Pt and intermediate adsorption and desorption sites. Thus, the overpotential was lowered to 27 mV to reach the current density of -10 mA cm<sup>-2</sup>, confirming the effective heterostructure engineering for HER.

On the other hand, the electric field-induced increased local reagent concentration was attractive for electrocatalytic processes. A high local electric field (LEF) can induce a local “pseudo-acidic” environment in an alkaline medium, which improves the electrocatalytic activity.<sup>[15]</sup> For instance, CoS<sub>2</sub> needle arrays were synthesized for HER.<sup>[16]</sup> The alkaline HER performance was enhanced due to the electric field-promoted H<sub>2</sub>O dissociation caused by the strong LEF around ordered needle arrays. Additionally, Yang’s group reported that the LEF at the tips of Pt-Ni nano-thorn arrays facilitated the selective adsorption and fast diffusion of H<sup>+</sup>, leading to boosting performances toward alkaline HER.<sup>[15c]</sup> The overpotential at current density of -10 mA cm<sup>-2</sup> reached 23 mV, showing the remarkable HER performance in the alkaline medium. However, most LEF was explored in tip-like shapes, other high curvature structures with LEF effects and higher density of active sites were less studied, not to mention building heterostructures on curvature structures. Because the high curvature structures are hard to be fabricated uniformly, meantime, the formation of heterostructure on the edge of high curvature structure is another difficulty.

Herein, we first synthesized transition metal phosphide (TMP) nanosheets as high curvature structure. TMP is recognized as a promising electrocatalyst owing to its unique electronic property from the modification of phosphorus.<sup>[17]</sup> Phosphating process can successfully introduce the P into transition metal electrocatalyst, constructing P-TM bonds, facilitating the HER kinetics.<sup>[18]</sup> Inspired by the HER performance and unique nanosheets structure, Ni<sub>2</sub>P/CoP nanosheets were chosen as the TMP substrate. Meantime, the high curvature of nanosheets with vertical structures can be a suitable substrate to load Pt on the edge, delivering an enhanced LEF effect for more active electrocatalysts, which is rarely studied in the HER field. After uniform TMP nanosheets were achieved, platinum nanocrystals were grown on the edge of TMP nanosheets by the electrodeposition. The orientation of nanosheets leads to an enhanced electric field on the edge and restricts the growth of Pt, leading to the uniform dispersion of Pt nanocrystals on the edge of nanosheet. The edge-induced localized electron

can accelerate the electrocatalytic process. Therefore, benefiting from the strong LEF, Pt nanocrystals on high curvature structures can concentrate more positively charged cations and facilitate the diffusion of H<sup>+</sup>.<sup>[7c,15c]</sup> Meantime, the synergistic effect between Pt and TMP results in an efficient water dissociation process and fast adsorption and desorption of protons. Thus, the unique heterostructure of Pt nanocrystals on the edge of TMP nanosheets can significantly accelerate adsorption and desorption of protons and increase the diffusion rate of H<sup>+</sup> with both synergistic and edge effects, boosting the HER performance in alkaline solutions.

## 2. Results and Discussion

Motivated by the remarkable HER performance of heterostructure catalysts and the exploration of LEF simulation on high curvature structures, we designed a strategy to grow Pt nanocrystals on the edge of transition bimetallic phosphides nanosheets with ultralow loading, as an efficient heterostructure for HER electrocatalyst.

### 2.1. Materials Synthesis and Characterization

Pt and TMP were combined as heterostructure electrocatalysts to boost the HER in an alkaline medium, named as Ni<sub>2</sub>P/CoP-Pt. Firstly, Ni<sub>2</sub>P/CoP nanosheets were fabricated through a two-step method, Ni(OH)<sub>2</sub> and Co(OH)<sub>2</sub> were fabricated on Ni foams through the electrodeposition process. Then, the as-prepared precursor was put in a tube furnace under nitrogen for phosphorating process at 350 °C, leading to the construction of Ni<sub>2</sub>P/CoP nanosheets, as reported in the previous work.<sup>[19]</sup> Second, Pt nanocrystals were grown on the edge of nanosheets by an electrodeposition method in a three-electrode cell with platinum foil and Ag/AgCl as counter and reference electrodes, respectively. The detailed synthesis was described in the supporting information. The schematic process is illustrated in **Figure 1**. Ni<sub>2</sub>P/CoP nanosheets were used as the substrate, after applying the current on the substrate, the distribution of the electric field was illustrated (Figure S1, Supporting Information). Detailed finite element method (FEM) simulation was described in the electric field part. The edge of the nanosheet has the strongest electric field caused by electrons in the whole nanosheet, which is consistent with the reported work.<sup>[20]</sup> Then, during electrodeposition process, Pt<sup>4+</sup> cations dissolved uniformly in the solution. The edge with the strongest electric field will attract more Pt<sup>4+</sup> cations than other areas, which is more favorable for reducing Pt<sup>4+</sup> cations during the electrodeposition process. Thus, the electric field distribution decides the growth area of Pt, forming small Pt nanoparticles on the edge. Finally, the unique structure of Pt nanocrystals grown on the edge of TMP nanosheets was realized. The uniform Ni<sub>2</sub>P/CoP nanosheets were shown in **Figure 2a** by scanning electron microscope (SEM). The vertical nanosheets with high curvature were the perfect substrate for loading Pt nanocrystals as heterostructure electrocatalysts. The high curvature of nanosheets can provide a large specific surface area, leading to more active sites, which

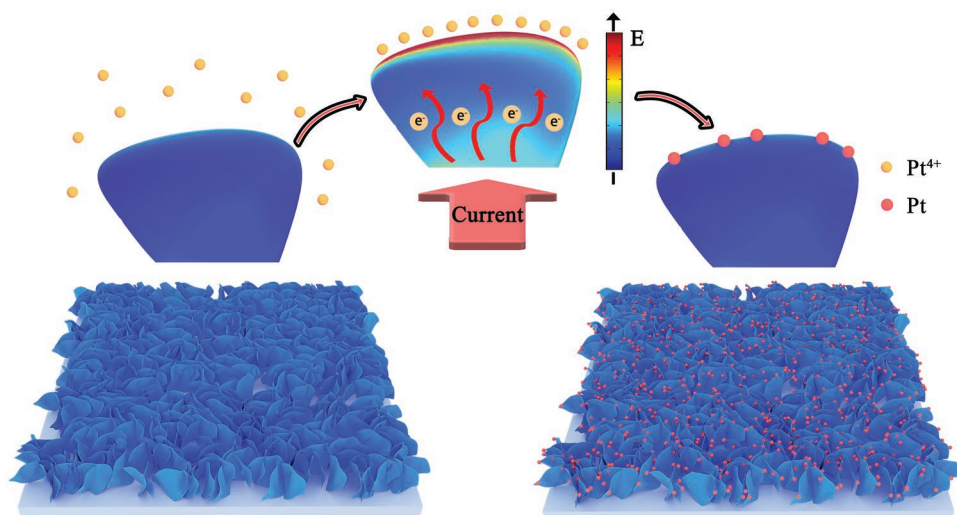


**Figure 1.** Schematic illustration of the growth of Pt nanocrystals on the edge of TMP nanosheets. (red arrow represents the movement of electrons; E represents the electric field).

is quite significant for electrocatalysts. Meantime, the vertical structure also ensures efficient gas release. Additionally, the vertical nanosheets with high curvature is a suitable model to study the enhanced local electric field for efficient HER. There were small Pt nanocrystals on the edge of nanosheets after 10 s electrodeposition, illustrated in Figure 2b, which confirmed the unique structure of Pt nanocrystals on the edge of TMP nanosheets. Due to the distribution of electric field on the nanosheet, Pt nanocrystals were grown mostly on the edge of the nanosheet, while a few Pt nanocrystals can be seen in the other areas of the nanosheet according to SEM observation.

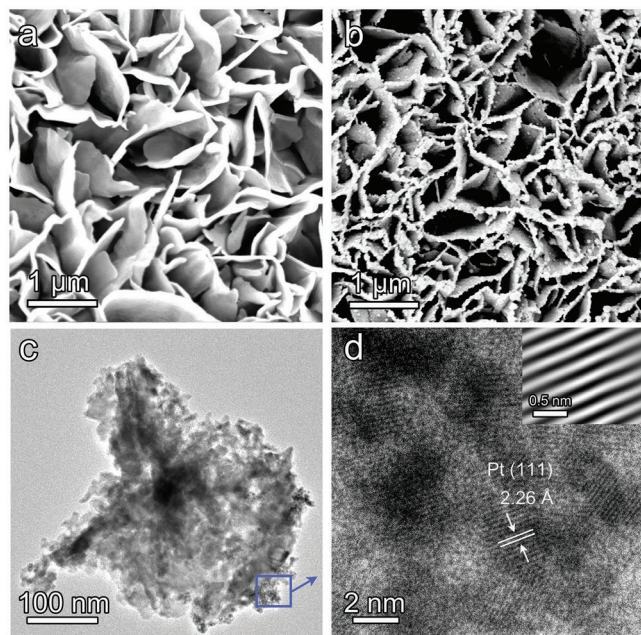


**Figure 2.** Morphology characterization. a) SEM image of  $\text{Ni}_2\text{P}/\text{CoP}$  nanosheet, b) SEM image and c) TEM image of  $\text{Ni}_2\text{P}/\text{CoP}-\text{Pt}$  10s. d) HRTEM image of Pt nanocrystals and inverse FFT filtered HRTEM image (inset).

A more detailed morphology was shown in the transmission electron microscopy (TEM) image. Figure 2c shows that  $\text{Ni}_2\text{P}/\text{CoP}$  nanosheets were surrounded by Pt nanocrystals. The high-resolution TEM (HRTEM) image shows the lattice space of 2.26 Å, corresponding to the (111) plane of Pt in Figure 2d. Inset figure illustrates the inverse fast Fourier transform (FFT) filtered HRTEM image of lattice fringes. Pt nanocrystals grown directly on the Ni foam are shown (Figure S2, Supporting Information). Pt nanocrystals show uniform dispersion on the Ni foam, because the electric field distribution on the smooth surface was uniform under the electrodeposition method.<sup>[21]</sup> While the distribution of Pt nanocrystals loaded on nanosheet was different, further illustrating the function of structural orientation of nanosheets, which lead to restrict the growth of Pt nanocrystals due to the high LEF. With the increase of electrodeposition time, Pt nanocrystals show different structures on TMPs. Pt nanocrystals will become large clusters on the edge after 50 s of electrodeposition. SEM images of  $\text{Ni}_2\text{P}/\text{CoP}-\text{Pt}$  with 50 s and 100 s of electrodeposition illustrate the morphology (Figure S3, Supporting Information). When increasing the electrodeposition time, the obvious aggregation of Pt is observed on the edge of nanosheet, but not other area. The diffusion of  $\text{Pt}^{4+}$  is uniform in the electrodeposition process, so there is a trend for the growth of Pt nanocrystals on the edge, which is caused by the strongest electric field on the edge, attracting the  $\text{Pt}^{4+}$ . The obvious aggregation of Pt in certain areas confirmed the preferable Pt growth on the edge of nanosheets due to the electric field distribution. The X-ray diffraction (XRD) patterns (Figure S4, Supporting Information) illustrate the successful fabrication of  $\text{Ni}_2\text{P}/\text{CoP}$  nanosheets on Ni foams. However, with ultra-low loading of Pt species, XRD patterns of the catalysts showed no obvious diffraction peaks from crystallized Pt metals or metal oxides.

To further explore the surface chemical composition, X-ray photoelectron spectroscopy (XPS) was used. The XPS survey spectrum (Figure S5, Supporting Information) presents the valence states and the compositional information of the heterostructure. The elements of Pt, Ni, Co, and P can be clearly

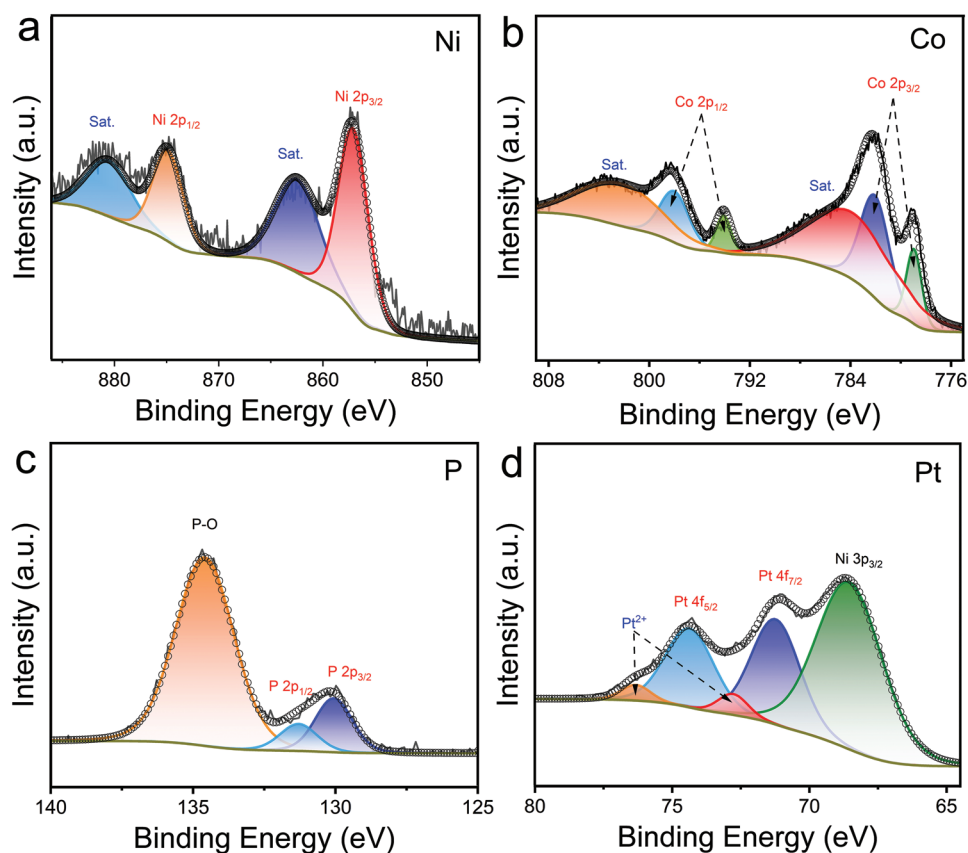


**Figure 3.** XPS spectra of a) Ni 2p, b) Co 2p, c) P 2p and d) Pt 4f of Ni<sub>2</sub>P/CoP-Pt heterostructure electrocatalyst.

identified. After the deconvolution, two peaks located at 857.1 eV and 874.9 eV correspond to Ni 2p<sub>3/2</sub> and Ni 2p<sub>1/2</sub> in Figure 3a.<sup>[22]</sup> The peaks at 862.6 eV and 880.7 eV can be ascribed to the satellite peaks. Figure 3b illustrates the XPS spectra of Co 2p, the peaks after the deconvolution at 778.9 eV and 782.2 eV are fitted to Co 2p<sub>3/2</sub>, while the peaks at 794.1 eV and 798.1 eV are assigned to Co 2p<sub>1/2</sub>. Another two peaks are satellite peaks, appearing at 784.6 eV and 802.5 eV.<sup>[23]</sup> XPS spectra of P 2p is illustrated in Figure 3c, the peaks at 130.0, 131.3, and 134.6 eV are corresponded to P 2p<sub>3/2</sub>, P 2p<sub>1/2</sub>, and oxidized metal phosphates, respectively. The oxidized metal phosphate peak is ascribed to the mild oxidation in air.<sup>[24]</sup> Figure 3d presents the XPS spectrum of Pt 4f. The paired peaks located at 71.3 eV and 74.4 eV correspond to metallic Pt<sup>0</sup>, indicating the formation of Pt nanocrystals.<sup>[25]</sup> The other peaks at 72.8 eV and 76.3 eV are ascribed to the Pt<sup>2+</sup> species, which is induced by oxidation when exposed in the air. Another peak at 68.6 eV represents the Ni 3p<sub>3/2</sub>.<sup>[13a]</sup> The chemical surface environment illustrates the successful formation of Pt nanocrystals on transition bimetallic phosphides.

## 2.2. Electrocatalytic Performances

The as-prepared electrocatalyst with heterostructure shows a remarkable HER activity in 1 M KOH. Commercial Pt/C, Ni foam, Ni foam-Pt, Ni<sub>2</sub>P/CoP and Ni<sub>2</sub>P/CoP-Pt with different

electrodeposition periods are examined to explore the advantages of heterostructures. Linear sweep voltammetry (LSV) curves with iR correction of Ni<sub>2</sub>P/CoP-Pt 10s, Ni<sub>2</sub>P/CoP-Pt 50s, and Ni<sub>2</sub>P/CoP-Pt 100 s are under the scan rate of 5 mV s<sup>-1</sup> (Figure S6, Supporting Information). At the current density of -10 mA cm<sup>-2</sup>, the overpotentials of Ni<sub>2</sub>P/CoP-Pt 10s, Ni<sub>2</sub>P/CoP-Pt 50s, and Ni<sub>2</sub>P/CoP-Pt 100s are 44.5, 31.5, and 24.1 mV, respectively. With an increasing loading amount of Pt nanocrystals, the HER performance increased, but the mass activity decreased (Figure S7, Supporting Information). The Pt mass percentages in Ni<sub>2</sub>P/CoP-Pt samples with the electrodeposition time of 10, 50, and 100s were examined by microwave plasma atomic emission spectrometers (MP-AES), which were 0.38, 0.71, and 0.96 wt%, respectively. At the potential of -0.07 V (vs RHE), the mass activities of Ni<sub>2</sub>P/CoP-Pt 10s, Ni<sub>2</sub>P/CoP-Pt 50s and Ni<sub>2</sub>P/CoP-Pt 100s are 2.77, 2.24, and 1.69 A mg<sup>-1</sup><sub>Pt</sub>, respectively. The aggregation of Pt nanocrystals leads to an overlap of active sites, in accordance with previous SEM observation (Figure S3, Supporting Information). By taking consideration of the cost, fabrication periods, and mass activities, the Ni<sub>2</sub>P/CoP-Pt 10 s has the highest value, which is more suitable for practical applications. LSV curves of commercial Pt/C, Ni foam, Ni foam-Pt 10s, Ni<sub>2</sub>P/CoP, and Ni<sub>2</sub>P/CoP-Pt 10s are shown in Figure 4a. The overpotentials at the current density of -10 mA cm<sup>-2</sup> for commercial Pt/C, Ni foam, Ni foam-Pt 10s, Ni<sub>2</sub>P/CoP, and Ni<sub>2</sub>P/CoP-Pt 10s are 44.2, 162, 90.9, 82.7, and 44.5 mV respectively. When the smooth Ni foam

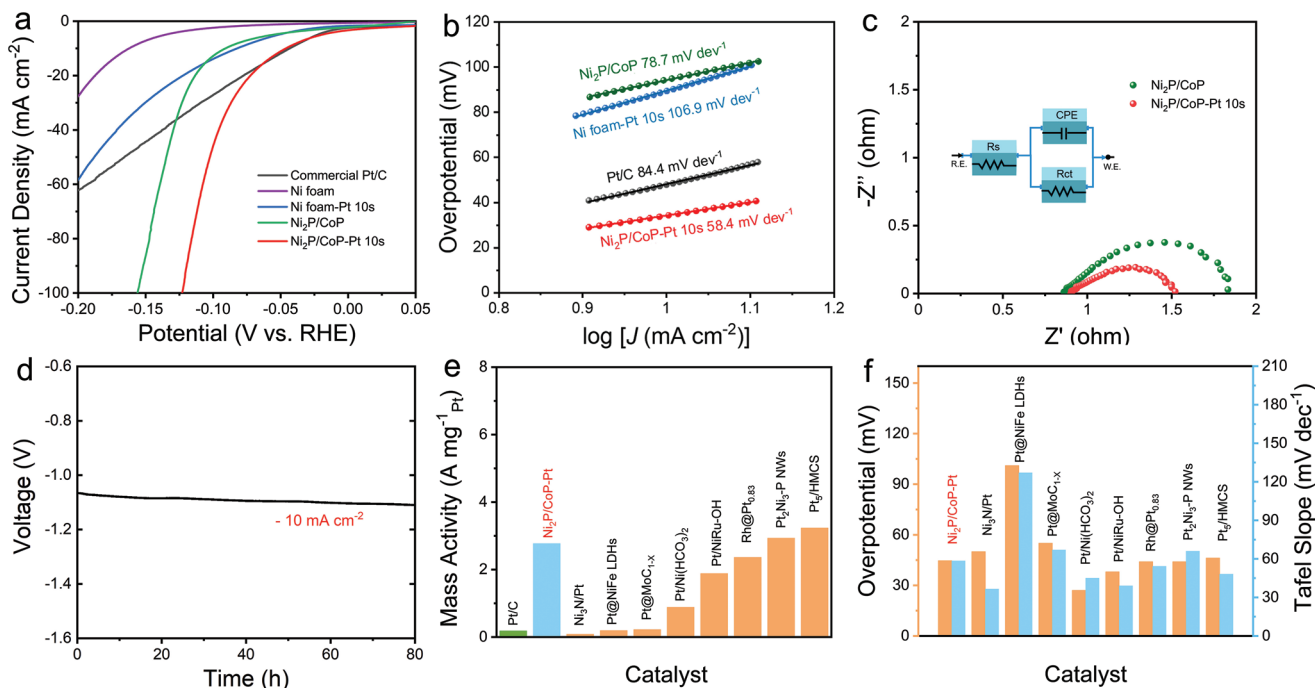


**Figure 4.** HER performance. a) LSV curves with iR correction of commercial Pt/C, Ni foam, Ni foam-Pt 10s, Ni<sub>2</sub>P/CoP, and Ni<sub>2</sub>P/CoP-Pt 10s. b) Tafel slopes of commercial Pt/C, Ni foam-Pt 10 s, Ni<sub>2</sub>P/CoP, and Ni<sub>2</sub>P/CoP-Pt 10s. c) Nyquist plots recorded at a voltage of  $-1.2$  V (vs Ag/AgCl) with an AC voltage of 5 mV over frequency range from 100 kHz to 0.1 Hz. Inset shows simulated equivalent circuit. d) Chronopotentiometry test of Ni<sub>2</sub>P/CoP-Pt 10 s. e) Mass activity of Pt and f) the comparison of overpotentials and Tafel slopes among other reported Pt nanocrystals-based electrocatalysts in an alkaline medium.

was loaded with Pt uniformly, the electrocatalyst illustrated limited HER performances. Then, the TMP nanosheets were loaded with Pt on the edge, the overpotential decreased to a low level, presenting both edge effect with local electric field and synergistic effects for HER in this unique heterostructure. The Tafel slopes of commercial Pt/C, Ni foam-Pt 10s, Ni<sub>2</sub>P/CoP and Ni<sub>2</sub>P/CoP-Pt 10s are 84.4, 106.9, 78.7, and 58.4 mV dec<sup>-1</sup>, respectively, as shown in Figure 4b, presenting the rate-limiting step of Volmer-Heyrovsky step. Electrochemical impedance spectroscopy (EIS) is explored in Figure 4c. The Nyquist plots of Ni<sub>2</sub>P/CoP and Ni<sub>2</sub>P/CoP-Pt 10s were acquired at voltage of  $-1.2$  V (vs Ag/AgCl) with an alternating current (AC) voltage of 5 mV over frequency range from 100 kHz to 0.1 Hz, corresponding to their respective onset HER overpotentials. The inserted figure shows a simulated circuit, which can reflect the resistance of charge transfer ( $R_{ct}$ ). Ni<sub>2</sub>P/CoP-Pt 10s shows smaller  $R_{ct}$  compared with Ni<sub>2</sub>P/CoP, indicating faster charge transfer with extra Pt loading. The electrochemical active surface area (ECSA) was studied by cyclic voltammetry (CV) with scan rates from 50 to 100 mV s<sup>-1</sup> (Figure S8, Supporting Information). The double-layer capacitance ( $C_{dl}$ ) of Ni foam-Pt 10s, Ni<sub>2</sub>P/CoP, and Ni<sub>2</sub>P/CoP-Pt 10s are 0.53, 46.7, and 68.1 mF cm<sup>-2</sup>, respectively (Figure S9, Supporting Information). The loading of Pt nanocrystals successfully increased the density of active sites. The durability was examined under a constant applied current density of  $-10$  mA cm<sup>-2</sup> for 80 h in Figure 4d. After 80 h test, the overpotential at the current density of  $-10$  mA cm<sup>-2</sup> increased from 39 to 79 mV. The SEM image (Figure S10a, Supporting Information) indicated the robust vertical structure of

Ni<sub>2</sub>P/CoP-Pt after 80 h catalytic process. Meantime, the high-angle annular bright-field-scanning transmission electron microscopy (HAABF-STEM) image (Figure S10b, Supporting Information) showed that Pt nanocrystals were on the edge of nanosheets, with no obvious change of sizes. The minor decrease of HER performance may be ascribed to the slight dissolution of Pt nanocrystals caused by the gas release. The mass activity of Ni<sub>2</sub>P/CoP-Pt 10s is 2.77 A mg<sup>-1</sup><sub>Pt</sub>, which is 15 times higher than that of commercial Pt/C with 0.18 A mg<sup>-1</sup><sub>Pt</sub> at potential of  $-0.07$  V (vs RHE). The mass activity of Pt at the potential  $-0.07$  V (vs RHE) along with the overpotential and Tafel slopes are ranked among the reported Pt nanocrystals-based electrocatalysts performed in 1 M KOH in Figure 4e,f, illustrating a remarkable performance. The detailed parameters are listed in Table S1 (Supporting Information). Moreover, as-prepared electrocatalysts show the same trend of HER performances in 1 M PBS and 0.5 M H<sub>2</sub>SO<sub>4</sub>, presenting their universal application (Figure S11, Supporting Information). After 10 s of electrodeposition for loading Pt on Ni<sub>2</sub>P/CoP nanosheets, the overpotentials decreased from 72.2 to 58.2 mV in 1 M PBS and 78.4 to 69.1 mV in 0.5 M H<sub>2</sub>SO<sub>4</sub> at a current density of  $-10$  mA cm<sup>-2</sup>.

### 2.3. Computational Simulation

Density functional theory (DFT) based first-principles calculations were performed to reveal the synergistic effect of HER over the Ni<sub>2</sub>P/CoP supported Pt catalysts. Three models, i.e., Pt (111), Ni<sub>2</sub>P/CoP (100) and Ni<sub>2</sub>P/CoP (100)/Pt surface (Figure S12,

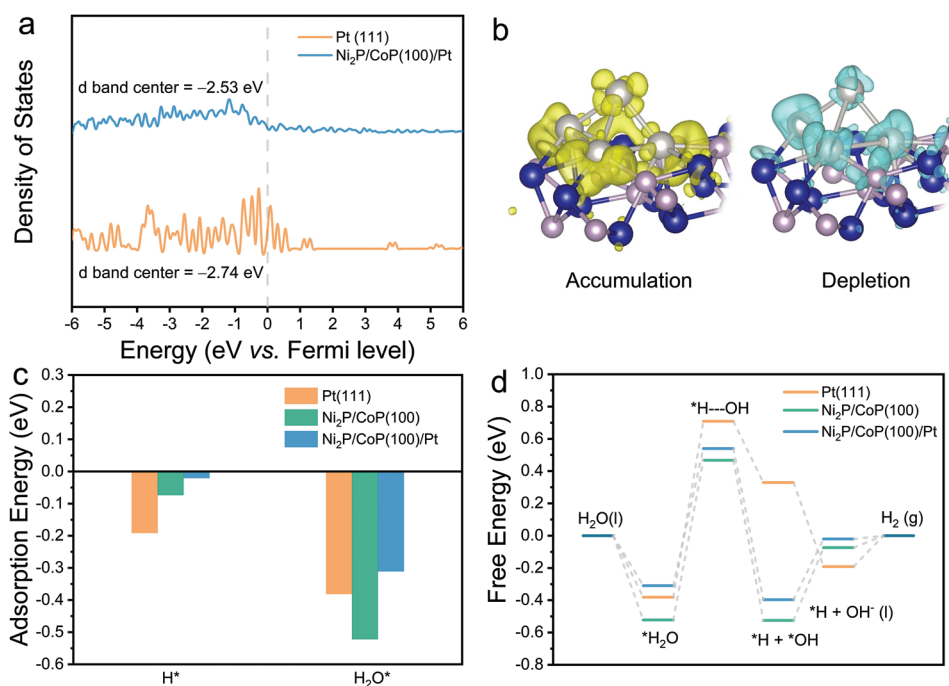


**Figure 5.** a) Projected density of states and *d*-band center of Pt 5*d* for Ni<sub>2</sub>P/CoP (100)/ Pt and Pt (111). b) Charge density difference of the Ni<sub>2</sub>P/CoP (100)/Pt interface, where yellow and cyan represent accumulation and depletion of charge density, respectively (white ball, Pt; blue ball, Co; Pink ball, P). c) Adsorption energy of H\* and H<sub>2</sub>O\* and d) Free energy diagram of hydrogen evolution over the surface of Pt (111), Ni<sub>2</sub>P/CoP (100) and Ni<sub>2</sub>P/CoP (100)/Pt.

Supporting Information) were firstly established. The Ni<sub>2</sub>P/CoP model was discussed in the previous work.<sup>[19]</sup> During the initial stage of the synthesis, the Pt<sub>4</sub> cluster was first formed on the edge, then became larger nanoclusters. Pt<sub>4</sub> used as the model can further understand the original synergistic effect between Pt and TMP. The binding energy of the Pt<sub>4</sub> cluster on the Ni<sub>2</sub>P/CoP (100) substrate was then calculated. Binding energy of 1.81 eV implies that the structure of Ni<sub>2</sub>P/CoP (100)/Pt is metastable in thermodynamics. The projected density of states (PDOS) of Pt in Pt (111) and Ni<sub>2</sub>P/CoP (100)/Pt surface (Figure 5a) were calculated. The *d*-band centers of Pt 5*d* in Pt (111) and Ni<sub>2</sub>P/CoP (100)/Pt surface are -2.74 and -2.53 eV, respectively. The peaks of PDOS in Ni<sub>2</sub>P/CoP (100)/Pt is enlarged and smoother, indicating that delocalization occurs between Pt cluster and phosphide substrate. A more positive *d*-band center suggests the adsorption might be weakened on Pt cluster, compared to Pt (111) surface. The charge density difference was provided in Figure 5b, which manifests that there are bonds generated between Pt-P and Pt-Co. From Bader charge analysis, it is known that there are 0.238 e transferred from phosphide substrates to Pt clusters, making Pt cluster more negatively charged active sites. The adsorption energies of H\* and H<sub>2</sub>O\* were calculated for these three models (Figure 5c). The adsorption geometries are provided (Figure S13, Supporting Information). The most positive adsorption energy of H\* appears at the top site of Ni<sub>2</sub>P/CoP (100)/Pt model, suggesting that Ni<sub>2</sub>P/CoP (100)/Pt model is more favorable for hydrogen desorption than Pt (111) and Ni<sub>2</sub>P/CoP (100) models. The adsorption of H<sub>2</sub>O\* of Pt cluster on Ni<sub>2</sub>P/CoP (100) is the weakest among three models. These results are in accordance with previously

calculated *d*-band centers. The activation energy for water dissociation is 1.09, 0.98, and 0.84 eV for Pt (111), Ni<sub>2</sub>P/CoP (100) and Ni<sub>2</sub>P/CoP (100)/Pt model, respectively. It is presented in the free energy diagram of the HER pathway in Figure 5d, from which the rate-determining step can be identified and the relationship between the composition and the activity can be elucidated. The activity follows the order of Ni<sub>2</sub>P/CoP (100)/Pt > Pt (111) > Ni<sub>2</sub>P/CoP (100). The rate-determining step is the dissociation of water on the catalytic surface in alkaline medium. The interactions between Pt cluster and phosphide substrate alleviate the strong adsorption of water, leading to a lower activation energy of water dissociation reaction. As for Pt nanocrystals, the activation energy of water dissociation and desorption of H\* were limited in alkaline medium, while combining with TMPs, both two important steps are boosted for an efficient HER process, confirming the successful synergistic effect in this strategy.

Finite element method simulation was applied to investigate the electric field distribution on the fabricated electrocatalysts through COMSOL. The 3D models were created as nanosheets and Pt nanocrystals using the statistics in Table S2 (Supporting Information). The slight change of thickness has little effect on the electric field distribution on the edge. The edge still has the strongest electric field. A voltage of -1.2 V was applied on the bottom of the nanosheet to simulate the experimental condition during the HER. For the electrodeposition process of Pt nanocrystals, a current of -10 mA cm<sup>-2</sup> was applied. Initially, in typical HER process, a single nanosheet was built up for simulation, the electric field distribution is taken from the Z-X plane (Figure S14a, Supporting Information). The edge of nanosheets shows the strongest electric field. Then electric field

distribution of Pt decorated nanosheets from the Z-X plane was illustrated (Figure S14b, Supporting Information). A high electric field occurs on the Pt nanocrystals. To see the electric field changes of these two models, the electric field distributions of cross-section models from Z-X plane were presented (Figures S14c and S14d, Supporting Information). A smooth and classic electric field distribution image was attained for a single nanosheet. Then a higher electric field variation on the Pt nanocrystals on the edge of nanosheet was observed. The electric field at the edge areas is further enhanced by the high geometric curvature with extra Pt loading, which is beneficial for faster diffusion of H<sup>+</sup> and accelerated reaction kinetics. The structural edge effects can result in a higher catalytic behavior, which is consistent with the experimental work.

### 3. Conclusion

In summary, we have developed a strategy to grow Pt nanocrystals on the edge of TMP nanosheets as a unique heterostructure electrocatalyst for efficient and robust HER in alkaline medium. The orientation of nanosheet lead to the unique heterostructure due to the electric field distribution. The HER performance was explored in both experimental and theoretical ways. The successful combination of Pt and TMP as unique structure shows not only the synergistic effect in boosting the kinetics in HER with efficient water dissociation, fast adsorption and desorption of protons, but also the edge effect in enhanced LEF, which is advantageous for faster diffusion of H<sup>+</sup>. The as-prepared electrocatalyst delivers an overpotential of 44.5 mV at the current density of -10 mA cm<sup>-2</sup> and 80 h durability. Meantime, the mass activity reaches to 2.77 A mg<sup>-1</sup><sub>Pt</sub>, which is 15 times higher than that of commercial Pt/C (0.18 A mg<sup>-1</sup><sub>Pt</sub>). Our work studies the heterostructure of Pt and TMP in synergistic effect and edge effect, pathing an innovative way to form the unique heterostructure and explore more possibilities for efficient nanostructured electrocatalyst for HER.

### Supporting Information

Supporting Information is available from the Wiley Online Library or from the author.

### Acknowledgements

The authors acknowledge China Scholarship Council/University College London for joint PhD scholarships, the project was supported by the Royal Society (RGS\R1\211080; IEC\NSFC\201261), Shanghai Scientific and Technological Innovation Project (22520710100), and Henan Overseas Expertise Introduction Centre for Discipline Innovation (CXJD2021003). The authors acknowledge Dr. David G. Hopkinson and Dr. Christopher S. Allen in electron Physical Science Imaging Centre at Diamond Light Source and the allocated experiment session (session ID MG30614, MG29809, MG32058).

### Conflict of Interest

The authors declare no conflict of interest.

### Author Contributions

Y.T. and G.H. conceived the project; Y.T. designed the experimental plan, synthesized the materials, and carried out electrochemical performance; J.F. performed the DFT calculation; H.D. performed the COMSOL simulation; Y.T., L.L., S.Z., F.L., Y.B., and T.L. contributed to materials characterization and data analysis; G.H. directed the project; G.H. and I.P. supervised students; Y.T. wrote the initial manuscript; All authors revised the manuscripts.

### Data Availability Statement

The data that support the findings of this study are available from the corresponding author upon reasonable request.

### Keywords

edge effect, heterostructure, hydrogen evolution reactions, platinum nanocrystals, transition metal phosphides

Received: August 28, 2022

Revised: October 29, 2022

Published online:

- [1] a) J. O. Abe, A. P. I. Popoola, E. Ajenifuja, O. M. Popoola, *Int. J. Hydrogen Energy* **2019**, *44*, 15072; b) R. Subbaraman, D. Tripkovic, D. Strmcnik, K.-C. Chang, M. Uchimura, P. Paulikas Arvydas, V. Stamenkovic, M. Markovic Nenad, *Science* **2011**, *334*, 1256.
- [2] a) S. Fang, X. Zhu, X. Liu, J. Gu, W. Liu, D. Wang, W. Zhang, Y. Lin, J. Lu, S. Wei, Y. Li, T. Yao, *Nat. Commun.* **2020**, *11*, 1029; b) N. Heinemann, J. Alcalde, J. M. Miocic, S. J. T. Hangx, J. Kallmeyer, C. Ostertag-Henning, A. Hassanpouryouzband, E. M. Thaysen, G. J. Strobel, C. Schmidt-Hattenberger, K. Edlmann, M. Wilkinson, M. Benthams, R. Stuart Haszeldine, R. Carbonell, A. Rudloff, *Energy Environ. Sci.* **2021**, *14*, 853; c) A. Chapman, K. Itaoka, K. Hirose, F. T. Davidson, K. Nagasawa, A. C. Lloyd, M. E. Webber, Z. Kurban, S. Managi, T. Tamaki, M. C. Lewis, R. E. Hebner, Y. Fujii, *Int. J. Hydrogen Energy* **2019**, *44*, 6371.
- [3] a) K.-J. Jeon, H. R. Moon, A. M. Ruminiski, B. Jiang, C. Kisielowski, R. Bardhan, J. J. Urban, *Nat. Mater.* **2011**, *10*, 286; b) Q. He, D. Tian, H. Jiang, D. Cao, S. Wei, D. Liu, P. Song, Y. Lin, L. Song, *Adv. Mater.* **2020**, *32*, 1906972.
- [4] a) S. Jiao, X. Fu, S. Wang, Y. Zhao, *Energy Environ. Sci.* **2021**, *14*, 1722; b) J. Wang, Y. Gao, H. Kong, J. Kim, S. Choi, F. Ciucci, Y. Hao, S. Yang, Z. Shao, J. Lim, *Chem. Soc. Rev.* **2020**, *49*, 9154.
- [5] a) Z. Lin, B. Xiao, Z. Wang, W. Tao, S. Shen, L. Huang, J. Zhang, F. Meng, Q. Zhang, L. Gu, W. Zhong, *Adv. Funct. Mater.* **2021**, *31*, 2102321; b) W. Li, Y. Liu, M. Wu, X. Feng, S. A. T. Redfern, Y. Shang, X. Yong, T. Feng, K. Wu, Z. Liu, B. Li, Z. Chen, J. S. Tse, S. Lu, B. Yang, *Adv. Mater.* **2018**, *30*, 1800676.
- [6] J. K. Nørskov, T. Bligaard, A. Logadottir, J. R. Kitchin, J. G. Chen, S. Pandelov, U. Stimming, *J. Electrochem. Soc.* **2005**, *152*, J23.
- [7] a) J. Ji, Y. Zhang, L. Tang, C. Liu, X. Gao, M. Sun, J. Zheng, M. Ling, C. Liang, Z. Lin, *Nano Energy* **2019**, *63*, 103849; b) C. Li, Z. Chen, H. Yi, Y. Cao, L. Du, Y. Hu, F. Kong, R. Kramer Campen, Y. Gao, C. Du, G. Yin, I. Y. Zhang, Y. Tong, *Angew. Chem. Int. Ed.* **2020**, *59*, 15902; c) D. Liu, X. Li, S. Chen, H. Yan, C. Wang, C. Wu, Y. A. Haleem, S. Duan, J. Lu, B. Ge, P. M. Ajayan, Y. Luo, J. Jiang, L. Song, *Nat. Energy* **2019**, *4*, 512.
- [8] Y. Gu, Y. Wang, J. Shi, M. Yang, Y. Rui, W. An, Y. Men, *Int. J. Hydrogen Energy* **2020**, *45*, 27067.

- [9] H. Yin, S. Zhao, K. Zhao, A. Muqsit, H. Tang, L. Chang, H. Zhao, Y. Gao, Z. Tang, *Nat. Commun.* **2015**, *6*, 6430.
- [10] Y. Tan, R. Xie, S. Zhao, X. Lu, L. Liu, F. Zhao, C. Li, H. Jiang, G. Chai, D. J. L. Brett, P. R. Shearing, G. He, I. P. Parkin, *Adv. Funct. Mater.* **2021**, *31*, 2105579.
- [11] Y. Kang, J. B. Pyo, X. Ye, R. E. Diaz, T. R. Gordon, E. A. Stach, C. B. Murray, *ACS Nano* **2013**, *7*, 645.
- [12] a) Y. Xie, J. Cai, Y. Wu, Y. Zang, X. Zheng, J. Ye, P. Cui, S. Niu, Y. Liu, J. Zhu, X. Liu, G. Wang, Y. Qian, *Adv. Mater.* **2019**, *31*, 1807780; b) P. Wang, K. Jiang, G. Wang, J. Yao, X. Huang, *Angew. Chem. Int. Ed.* **2016**, *55*, 12859.
- [13] a) M. Lao, K. Rui, G. Zhao, P. Cui, X. Zheng, S. X. Dou, W. Sun, *Angew. Chem. Int. Ed.* **2019**, *58*, 5432; b) I. T. McCrum, M. T. M. Koper, *Nat. Energy* **2020**, *5*, 891.
- [14] A. Alinezhad, L. Gloag, T. M. Benedetti, S. Cheong, R. F. Webster, M. Roelsgaard, B. B. Iversen, W. Schuhmann, J. J. Gooding, R. D. Tilley, *J. Am. Chem. Soc.* **2019**, *141*, 16202.
- [15] a) H. Li, C. Cai, Q. Wang, S. Chen, J. Fu, B. Liu, Q. Hu, K. Hu, H. Li, J. Hu, Q. Liu, S. Chen, M. Liu, *Chem. Eng. J.* **2022**, *435*, 134860; b) G. Zhou, Y. Hu, L. Long, P. Wang, Y. Shan, L. Wang, J. Guo, C. Zhang, Y. Zhang, L. Liu, *Appl. Catal., B* **2020**, *262*, 118305; c) A. Nairan, C. Liang, S.-W. Chiang, Y. Wu, P. Zou, U. Khan, W. Liu, F. Kang, S. Guo, J. Wu, C. Yang, *Energy Environ. Sci.* **2021**, *14*, 1594.
- [16] G. Chen, H. Li, Y. Zhou, C. Cai, K. Liu, J. Hu, H. Li, J. Fu, M. Liu, *Nanoscale* **2021**, *13*, 13604.
- [17] a) J. Kibsgaard, C. Tsai, K. Chan, J. D. Benck, J. K. Nørskov, F. Abild-Pedersen, T. F. Jaramillo, *Energy Environ. Sci.* **2015**, *8*, 3022; b) Y. Shi, B. Zhang, *Chem. Soc. Rev.* **2016**, *45*, 1529; c) M. Sun, H. Liu, J. Qu, J. Li, *Adv. Energy Mater.* **2016**, *6*, 1600087.
- [18] a) C.-C. Weng, J.-T. Ren, Z.-Y. Yuan, *ChemSusChem* **2020**, *13*, 3357; b) X. Yang, A.-Y. Lu, Y. Zhu, M. N. Hedhili, S. Min, K.-W. Huang, Y. Han, L.-J. Li, *Nano Energy* **2015**, *15*, 634; c) G. Huang, W. Liang, Y. Wu, J. Li, Y. Q. Jin, H. Zeng, H. Zhang, F. Xie, J. Chen, N. Wang, Y. Jin, H. Meng, *J. Catal.* **2020**, *390*, 23.
- [19] Y. Tan, J. Feng, L. Kang, L. Liu, F. Zhao, S. Zhao, D. J. L. Brett, P. R. Shearing, G. He, I. P. Parkin, *Energy Environ. Mater.* **2022**, <https://doi.org/10.1002/jeem2.12398>.
- [20] a) P. R. Sajanlal, C. Subramaniam, P. Sasanpour, B. Rashidian, T. Pradeep, *J. Mater. Chem.* **2010**, *20*, 2108; b) M. Liu, Y. Pang, B. Zhang, P. De Luna, O. Voznyy, J. Xu, X. Zheng, C. T. Dinh, F. Fan, C. Cao, F. P. G. de Arquer, T. S. Safaei, A. Mepham, A. Klinkova, E. Kumacheva, T. Filleter, D. Sinton, S. O. Kelley, E. H. Sargent, *Nature* **2016**, *537*, 382; c) D. Ghoshal, A. Yoshimura, T. Gupta, A. House, S. Basu, Y. Chen, T. Wang, Y. Yang, W. Shou, J. A. Hachtel, J. C. Idrobo, T.-M. Lu, S. Basuray, V. Meunier, S.-F. Shi, N. Koratkar, *Adv. Funct. Mater.* **2018**, *28*, 1801286; d) M. Jalali, R. S. Moakhar, T. Abdelfattah, E. Filine, S. S. Mahshid, S. Mahshid, *ACS Appl. Mater. Interfaces* **2020**, *12*, 7411.
- [21] a) L. Zhang, J. Wan, J. Li, Q. Cui, D. He, C. Zhao, H. Suo, *J. Electrochem. Soc.* **2020**, *167*, 027537; b) M. A. Kamyabi, K. Ebrahimi-Qaratapeh, M. Moharramnezhad, *J. Porous Mater.* **2021**, *28*, 393.
- [22] Y. Zhang, Y. Liu, M. Ma, X. Ren, Z. Liu, G. Du, A. M. Asiri, X. Sun, *Chem. Commun.* **2017**, *53*, 11048.
- [23] C. Guan, W. Xiao, H. Wu, X. Liu, W. Zang, H. Zhang, J. Ding, Y. P. Feng, S. J. Pennycook, J. Wang, *Nano Energy* **2018**, *48*, 73.
- [24] X. Zhang, X. Yu, L. Zhang, F. Zhou, Y. Liang, R. Wang, *Adv. Funct. Mater.* **2018**, *28*, 1706523.
- [25] S. Jeong, H. D. Mai, K.-H. Nam, C.-M. Park, K.-J. Jeon, *ACS Nano* **2022**, *16*, 930.